RESEARCH

Effect of Ionic Liquid Anions in Tunning the Morphology and Size of Ag in rGO-Ag Nanocomposites: Anticancer Activity of the Composites Against A549 Lung Cancer Cells

K. Lakshmanamoorthy[1] · S. Prabhu[2] · V. Ravikumar[2] · S. Manivannan[1]

Abstract

Here, we report the cytotoxicity properties of silver nanostructure—reduced graphene oxide composites (rGO-Ag) prepared with different ionic liquids (ILs). The role of ILs anions in tuning the morphologies of Ag (nanoparticles, wires, and rods) on the rGO was studied. The 1-butyl-3-methylimidazolium methylsulfate acts as an effective additional surfactant for the formation of lengthy silver nanowires (rGO-Ag4). The ILs play a significant role in the morphologies of silver nanostructures, which in turn highly determine the cytotoxicity of prepared composites against the A549 lung cancer cell lines. With the standard methyl-thiazole-tetrazolium (MTT) assay, an IC_{50} value of 20 µg/mL was obtained for biocompatible rGO-Ag composite prepared using 1-butyl-3-methylimidazolium trifluoroacetate (BMIM TFA), which is found to be equivalent (i.e. 20 µg/mL) for bare Ag. The morphological evolution of A549 cells was carefully examined in the acridine orange/ethidium bromide dual stain. Further, the reactive oxygen species production, a controlling factor of cytotoxicity was studied by DCFH-DA stain, whereas nucleus condensation/fragmentation was probed with Hoechst 33258 stain. It is shown that the rGO-Ag composite prepared with BMIM TFA IL can be effectively used for cytotoxic activity toward A549 cells, due to the effective release of Ag^+ ions into the intracellular region and the mechanism is discussed in detail.

Keywords Graphene oxide · Silver nanowires · Particles · Ionic liquids · A549 cells · Cytotoxicity

1 Introduction

In recent times, cancer becomes a common disease and identified as a severe threat to humanity. Among its various types, lung cancer is found to be the second most observed menace. With a high mortality rate of 18%, it is a major concern that needs to be addressed imminently [1]. Typically, lung cancer cells are categorized as (i) small cell carcinoma and (ii) non-small cell carcinoma cells, where the former covers 85% of the reported cases. Factors like smoking, exposure to radiation into the lungs, genetic factors, toxins, particle pollution, lack of exercise and stress may lead to such disease. Oncologists decide the treatment method based on the cancer stage, patient's age and performance score [2]. Though chemotherapy is commonly used method for treating earlier-stage tumor, it has side effects, due to the poor biocompatibility of the drugs used which cannot be avoided [3]. Nanomaterials could be a better alternative to these conventional chemotherapy drugs, with an advantage of improved cytotoxicity upon minimal drug load. Of these, carbon-based nanomaterials are effective due to its biocompatibility and drug-carrying ability [4].

Graphene-based materials have gained significant attention in recent times for their reliable electrical, optical, mechanical and thermal properties [5–7]. The presence of localized π-electrons in the sp^2 bonded carbon structures are widely used in energy storage/harvesting, sensing, electronic, optoelectronic, thermal, biosensing, and biomedical applications [8–11]. The 2-dimensional graphene oxide (GO)/ reduced graphene oxide (rGO) are suitable in biomedical applications, because oxygen functional groups present in these structures enhances their properties. Oxygen functional groups serve as the spots to attach different bioactive

✉ S. Manivannan
  ksmani@nitt.edu

1 Carbon Nanomaterials Laboratory, Department of Physics, National Institute of Technology, Tiruchirappalli 620 015, India

2 Department of Biochemistry, School of Life Science, Bharathidasan University, Tamil Nadu, Tiruchirappalli 620 024, India

materials and drug molecules over rGO structures [12]. In recent reports GO and rGO show cytotoxicity against cancer cells with greater loading. By producing excessive reactive oxygen species (ROS) in cancer cells causes the oxidative stress, which will result to the death of the cancer cells. GO/rGO shows low cytotoxicity against cancer cells compared to other materials like metal-based nanostructures. This impediment of low cytotoxicity against cancer cells can only be addressed by making composites with suitable materials.

Historically, silver is known for its therapeutic properties [13]. In modern times silver nanoparticles (AgNPs) found their applications in anti-cancer, antibacterial, biosensing and bioimaging [14, 15]. Cytotoxicity of AgNPs is highly reliant on their size and morphology. The small-sized AgNPs are adsorbed on cell membrane and induce oxidative stress by producing ROS which leads to apoptosis [16]. However, long-time ingestion of silver will cause a disease condition called argyria [17]. To reduce the amount of silver administration in treatment process, targeted release of silver to cancerous tissues is essential. This can be achieved by employing GO/rGO as carriers [18]. For the past few years, GO-AgNPs and rGO-AgNPs composites are used for anti-cancer activity applications due to their improved biocompatibility [19–21]. Different physical and chemical methods are available to prepare rGO-AgNPs composites, among which polyol-based chemical reduction methods are widely used. To tune the morphology of Ag decorated over rGO is achieved by varying the reaction conditions like concentration of $AgNO_3$, temperature, mode of reduction, reducing agents and surfactants used. One pot synthesis of AgNWs-rGO composites with Abelmoschus esculentus plant extract as reducing agent, for nitroarene reduction [22], had a spiral morphology with low aspect ratio, which is not suitable for certain applications. Albeit their good sensitivity against ascorbic acid, dopamine and uric acid, recent AgNWs-rGO based electrochemical biosensors requires multiple steps in their synthesis [23]. Even though, these AgNW-rGO composites are demonstrated for various potential applications [24–26], their long preparation time, agglomeration of silver and inability to control the morphology of silver need to be fixed.

To overcome the aforementioned difficulties, in the present work, we adopted a one-pot microwave-assisted synthesis method. Here, rGO-silver nanocomposites with tunable morphologies of silver nanostructures decorated on rGO sheets are reported. To ascertain this, imidazolium and pyrrolidone cations-based ionic liquids (ILs) were utilized. There are many possible combinations of cations and anions that can be used to design ILs, a good deal of room temperature ILs are available [27]. Growth and morphologies of the nanostructures prepared in ILs are depends on the length of alkyl chain in IL cation and nature of the anion. In recent times, ILs are used to covalently modify GO/rGO structures,

as well as to prepare tunable metal nanostructures due to their low vapor pressure, high viscosity, high boiling point, and high chemical and thermal stabilities [28, 29]. Cytotoxicity of the prepared samples was tested against A549 lung cancer cells.

2 Experimental Techniques

2.1 Preparation of GO and Ionic Liquids

The modified Hummers method was adapted to synthesize GO [30]. The ILs 1-butyl-3-methylimidazolium tetrafluoroborate (BMIM BF_4), 1-butyl-3-methylimidazolium trifluoroacetate (BMIM TFA), 1-butyl-3-methylimidazolium methylsulfate (BMIM $MeSO_4$) and N-methyl-2-pyrrolidone hydrogen sulfate (NMP HSO_4) were prepared by following the previously described synthesis methods [31, 32].

2.2 Preparation of rGO-Ag Composites

Two-steps process was adapted to synthesize rGO-Ag composites. Initially, three different stock solutions were prepared. Solution (A): 0.3 M of $AgNO_3$ in 36 ml ethylene glycol (EG) in a 100 mL beaker stirred for an hour at 27 °C. Solution (B): 1.8 M of PVP + 4.3 mg of $FeCl_2.H_8O_4$ in 36 mL EG in 250 ml beaker and stirred for an h at 80 °C and the solution turned to a pale yellow. Solution (C): 108 mg of GO in 36 mL of EG sonicated for an hour at 27 °C.

In the first step, solution (B) was allowed to cool to 27 °C, then solution (C) was added to it and sonicated for 30 min to attain dispersion. The solution was then treated with microwave irradiation for 2 min at 360 W after the addition of 50 μL of solution (A). Once the above seed solution cooled to 27 °C, 14 mL of the seed solution was transferred to a 100 mL beaker in five sets. Different ionic liquids of each 5 μL were added to the above solutions (rGO-Ag1-without adding IL, rGO-Ag2 with the addition of BMIM BF_4, rGO-Ag3 with the addition of BMIM TFA, rGO-Ag4 with the addition of BMIM $MeSO_4$, and rGO-Ag5 with the addition of NMP HSO_4) and sonicated for 5 min which was then MW irradiated for 3 min at 360 W. The solution was then allowed to cool to 27 °C and was washed using water, ethanol and acetone through centrifugation at a relative centrifugal force (RCF) of 4226×g to collect the samples.

2.3 Synthesis of rGO and Ag

To synthesize Ag, 7.2 mL of the stock solution (A) and 7.2 mL of the solution (B) were taken in 100 mL beaker and were MW treated for 3 min at 360 W. Then, washed using acetone, water, and ethanol through centrifugation at RCF of 1304×g (6000 rpm). To prepare rGO, 7.2 mL of 1.8 M

PVP solution and 7.2 mL of 3 mg/mL GO solutions were taken in a 100 mL beaker and were MW treated for 3 min at 360 W. The solution was allowed to cool to 27 °C and washed using acetone, water, and ethanol by centrifugation at RCF of 4226×g.

2.4 Cell Culture

The National Centre for Cell Science, Pune, India supplied the NCI-A549 lung cancer cell lines. The obtained cells were further cultured in Dulbecco's modified Eagle's medium accompanied with fetal bovine serum (10% v/v) and 1% penicillin/streptomycin at 37 °C with a 5% CO_2 atmosphere. Using trypsin-EDTA the stock cultured cells were harvested which were then sub-cultured for further use.

2.5 Cytotoxicity Assay

In this study, cytotoxicity of the synthesized samples was assessed by the methyl-thiazole-tetrazolium (MTT) assay. For this, 96 well plates (1×10^4 cells/well) were used to grow the obtained cells. GO, rGO, Ag and rGO-Ag samples stock solution in the non-toxic solvent and diluted to a final working solution with incomplete media. The NCI-A549 cells were exposed to the prepared nanomaterials with different concentrations (1–10 μg/mL). Triplicates were prepared for all concentrations including untreated cells as control, all maintained at the same condition. After treatment, 24 h of incubation, 20 μL of MTT solution was added to each well [Dimethyl thiazolyltetrazolium bromide, 5 mg/mL in (1xPBS)] (Hi Media Laboratories, Mumbai, India). Then, the culture plates were incubated at 37 °C for 4 h, after which it was covered with aluminum foil. After removal of culture media, 200 μL of DMSO was added to each well to dissolve formazan. Microplate reader (Bio-rad, USA) was assisted to quantify the absorbance at 595 nm. The inhibition percentage was calculated by accounting the results obtained for triplicates with the formula:

$$= \frac{[Mean\ Optical\ Density(OD)\ of\ control\ cells - Mean\ OD\ of\ nanoparticles\ salted\ cells]}{Mean\ OD\ of\ control\ cells} X100 \quad (1)$$

2.6 Analyzing the Morphological Changes of Cancer Cells by AO/EB Staining

To stain both the live and lifeless cells, acridine orange (AO), a vibrant dye was used to study the morphologies of the cells. Ethidium bromide (EB) was used to stain only the cells that vanished their membrane integrity [33]. To quantify the level of apoptosis in NCI-A549 cells upon treated with the prepared samples, 6-well plates were used with seeded cell concentrations of 1×10^5 cells/well. After

attaining 60% confluency of seeded cells, the prepared samples were introduced and further allowed to incubate for 24 h. After the incubation time, EB/AO (50 μL/mL) dual stain was introduced with the incubated cells and maintained at 37 °C for 30 min under a 5% CO_2 atmosphere. To eliminate the excess dye the stained cells were washed with 1×PBS. To capture the images of apoptotic cells, 40×objectives in a fluorescence microscope (FLoid Cell Imaging Station, Life Technologies, USA) was used.

2.7 Measurement of ROS

Dysfunction of mitochondria will lead to overproduction of ROS, which will lead to changes in the intracellular signaling pathways [34]. ROS generation in NCI-A549 cells was evaluated by fluorescence microscopy. To quantify the level of ROS in NCI-A549 cells, the 6-well plates were used with seeded cells concentration of 1×10^5. After reaching 60% confluency, rGO-Ag composites were allowed to incubate for 24 h. Following the incubation period, cells are stained with 40 μM DCFH-DA (Sigma-Aldrich, Bangalore, India) for 30 min. To eliminate the excess dye from the stained cells, 1×PBS was used to wash. The 40×objectives were used to record images of the cells under a fluorescence microscope.

2.8 Nuclear Staining Analysis by Hoechst 33258

Hoechst 33258 produced strong fluorescence after binding with the nucleus in dead and living cells [35]. To analyze the nucleus of apoptotic NCI-A549 cells, the 6-well culture plates were used with seeded cells concentration of 1×10^5/mL. After attainment 60% confluency, rGO-Ag composites were added to the plates. Later the 24 h of incubation, 50 μL/mL of Hoechst 33,258 stain was introduced into it and incubated in a 5% CO_2 atmosphere at 37 °C for 30 min. Fluorescence images of the cells were recorded with 40×objectives in a fluorescence microscope.

3 Results and Discussion

Figure 1a, shows the powder XRD patterns of prepared samples. GO shows two peaks at 11.26° and 42.80° corresponding to (001) and (101) planes of graphitic carbon, respectively. The peak at 11.26° is evidenced for the complete oxidation of graphite. In rGO, a wide peak centered at about 23.50° is for the (002) plane of graphitic carbon. A low-intensity broad peak is evidenced for the reduction of GO to rGO. The peaks for prepared Ag appeared at 38.50°
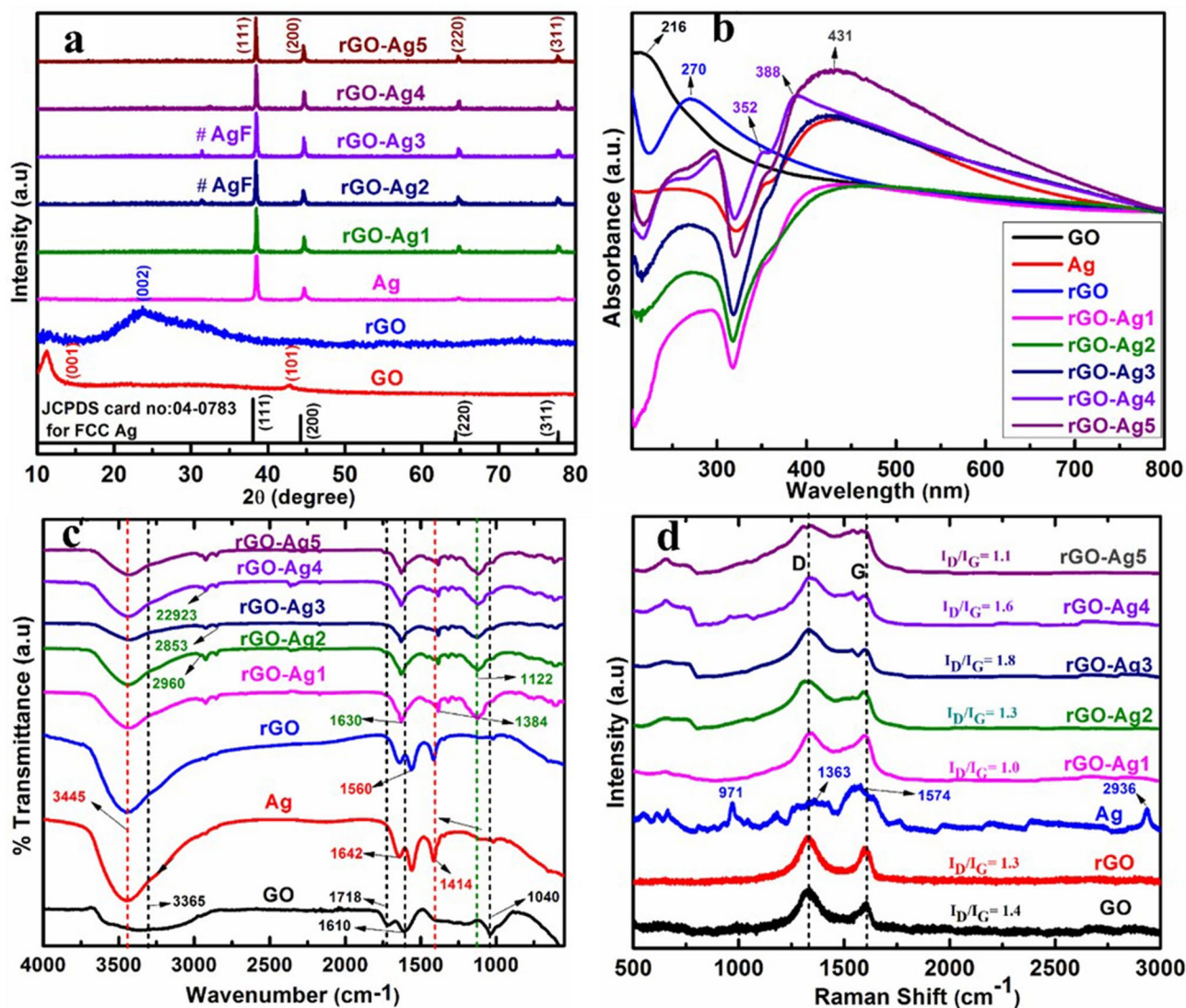
Fig. 1 **a** Powder XRD patterns **b** UV–Visible absorption spectra, **c** FT-IR spectra and **d** Micro-Raman spectra of the prepared samples

(111), 44.70° (200), 64.80° (220) and 77.80° (311). The XRD pattern of prepared Ag matches with the JCPDS data corresponding to FCC silver. By fitting the XRD data, the areal intensity of peaks are calculated, and the fitted curves are shown in supporting information (SI) Fig. SF1. The areal intensity ratio of planes (111)/(200) are calculated as 2.21, 2.28, 1.99, 1.97, and 2.03 for composites rGO-Ag1-5, respectively. It is also important to note that the intensity ratio for planes (200)/(220) are 2.50, 2.02, 2.16, 2.75, and 2.60 for the composites rGO-Ag1-5, respectively. Here, rGO-Ag4 has the highest value of 2.75, indicating the formation of nanowires (Table ST1, SI).

An absorption peak at 216 nm, originated from the π–π* electronic transitions of aromatic C–C bonds in GO (Fig. 1b) is noticed. An additional weak absorption at

290 nm is observed for n–π* transitions of C=O bonds. In rGO spectrum, the peak originated from π–π* of aromatic C–C shifted to a higher wavelength of 270 nm, and complete disappearance of n–π* are due to the reduction of GO and refurbishment of sp² electronic structure of graphite [7]. This is consistent with FT-IR results, there exhibits the evidences for suppression of C=O vibrations in rGO. Silver nanostructures show three prominent surface plasmon resonance (SPR) absorptions at UV–Vis spectral region. The peak around 350 nm is longitudinal SPR for nanowires. And it shows transverse SPR at around 380 nm corresponding to nanowires. A broad peak around 430 nm is for SPR of nanoparticles [36]. The prepared Ag shows two SPR absorptions at 354 nm and 437 nm (maximum intensity), indicating the formation of more nanoparticles along with a few nanorods.

The sample rGO-Ag4 shows peaks corresponding to silver nanowires, like the longitudinal and transverse SPR at 352 and 388 nm, respectively. The samples rGO-Ag1, rGO-Ag3, and rGO-Ag5 show absorption peaks around 430 nm corresponding to the nanoparticles. Sample rGO-Ag2 did not show any absorption at 352 nm but showed a peak at 461 nm supporting the formation of nanoparticles. Together with the SPR absorptions of nano silver, electronic transitions corresponding to C–C bonds also appeared in rGO-Ag samples. The rGO (270 nm) absorptions are redshifted, and centered at 293, 277, 271, 297 and 296 nm for composites rGO-Ag1-5, respectively. The shift is more in the case of rGO-Ag1, rGO-Ag4 and rGO-Ag5 compared to rest of the composites. This is due to the changes occurs after interaction of nanoparticles with rGO. These changes are guided by the addition of ionic liquids. The Tauc plot is used to calculate the band gap of the prepared samples and the relation is given in Eq. 2 and the plots are shown in SI (Fig.SF2).

$$(\alpha h\nu)^n = A\left(h\nu - E_g\right) \qquad (2)$$

Here, α- absorption coefficient, $h\nu$- energy of photons, A- proportionality constant, E_g- band gap of the material, n- power factor (n = 2 for direct band gap). By extrapolating the absorption edges to the x- axis, the band gap of 4.36 eV, 5.66 eV, 5.03 eV, 4.58 eV, 5.13 eV, 5.44 eV and 5.91 eV for the samples GO, rGO, rGO-Ag1, rGO-Ag2, rGO-Ag3, rGO-Ag4 and rGO-Ag5, respectively. In rGO-Ag3, rGO-Ag4 and rGO-Ag5 plasmonic absorption of silver nanostructures was noticed which is shown in SI (Fig.SF2).

FT-IR vibrational spectra of prepared samples are given in Fig. 1c, and the appeared vibrational bands and their assigned functional groups are given in Table 1. The carbonyl groups in GO are act as nucleating sites for the evolution of nanosilver [37]. Weak bands observed at wavenumbers lower than 1000 cm^{-1} are validates for the existence of silver in the prepared composites.

To further quantify the functional groups present in the prepared samples, spectrum is analyzed between 900 and 1900 cm^{-1} adapting the procedure reported elsewhere [39]. The deconvoluted spectra of prepared samples are shown in SI (Fig.SF3), the functional group assignments are made, and their areal intensities are calculated [40]. Fraction of C = O functional groups present in the prepared samples are calculated from the FT-IR spectra using the following formula,

$$\text{Fraction of (C = O) groups } = \frac{Area\ of\ C = O\ functional\ group}{Area\ of\ all\ functional\ groups} \qquad (3)$$

The calculated values are 0.12, 0.33, 0.33, 0.32, 0.44, 0.37, 0.39 and 0.33 for the samples GO, Ag, rGO, rGO-Ag1, rGO-Ag2, rGO-Ag3, rGO-Ag4 and rGO-Ag5,

Table 1 Band assignments for FT-IR spectra of prepared samples

Wavenumber (cm^{-1})	Functional groups and mode
1040	ν_s(C–O–C) [38]
1610	ν_s (C = C)
1718	ν_s (C = O)
3365, 3445	ν_s (O–H) [38]
1414	β(CH)
1560	δ(N–H)
1639	ν_s (C = O)
2852	ν_s(C–H)
2922	ν_{as} (C–H)
1384	β (C–H)
2960	β (C–H)
1122	ν_s (C–O)
< 1000	ν(O–Ag$^+$) [37]

ν_s-symmetric stretching, ν_{as} -asymmetric stretching, β-deformation and δ-bending vibrations

respectively. The increased fraction of C = O in Ag, rGO and composites compared to that of GO is due to the presence of PVP surfactant, which in turn improves biocompatibility of the composites.

Figure 1d displays the micro-Raman spectra for the prepared samples. GO has two characteristic bands centered at 1324 cm^{-1} (D band for the disorder induced k-point phonons of A$_{1g}$ symmetry vibrations of sp^3 carbon structures) and at 1602 cm^{-1} (G band for the first-order scattering of E$_{2g}$ mode of sp^2 carbons). The I$_D$/I$_G$ ratio calculated from the peak intensity of D and G bands are 1.4, 1.3, 1.0, 1.3, 1.8, 1.6 and 1.1 for GO, rGO, rGO-Ag1, rGO-AG2, rGO-Ag3, rGO-Ag4 and rGO-Ag5, respectively. Except for rGO-Ag3 and rGO-Ag4, all other samples have a lower I$_D$/I$_G$ ratio than GO. The crystallite size of graphene sheets in lateral direction was calculated from the I$_D$/I$_G$ ratio by Tuinstra–Koenig (T-K) relation [41]. The T-K equation relates the crystallite size with I$_D$/I$_G$ as,

$$La(nm) = \frac{\left(2.4 \times 10^{-10}\right)(\lambda)^4}{(I_D/I_G)} \qquad (4)$$

Here, λ is the wavelength of the laser used (532 nm). The crystallite size calculated from the I$_D$/I$_G$ ratio of the samples are 13.73, 14.79, 19.23, 14.79, 10.68, 12.02 and 17.48 for GO, rGO, rGO-Ag1, rGO-AG2, rGO-Ag3, rGO-Ag4 and rGO-Ag5, respectively. To further analyze the PVP capping in prepared composites through Raman spectra, curve fitting was done and shown in SI (Fig.SF4). The detailed discussion was done in the supporting information under the section micro-Raman analysis.

FE-SEM image of GO is given in Fig. 2a, GO sheets are agglomerated and appeared as blurred images, due to the less conducting nature of GO. In rGO, sheets are much more visibly observed, because of their improved conductivity, by the partial removal of functional groups. The sheets are stacked together after the reduction and appear as a wavy structure (Fig. 2b). In Ag (Fig. 2c), small rods are grown from nanoparticles. In sample rGO-Ag1 (Fig. 2d) nanorods and nanoparticles are decorated on rGO. Sample rGO-Ag2 project (Fig. 2e) the rGO decorated with silver nanoparticles at the edges. Silver nanoparticles are decorated throughout the rGO sheets in rGO-Ag3 and no rod/wires were observed (Fig. 2f). Long wires are formed on rGO sheets along with particles in rGO-Ag4 (Fig. 2g). The average thickness of the wires is measured as 110 nm (Fig. 2i). The sample rGO-Ag5 is shown in Fig. 2h, in which, the silver nanoparticles and rods are decorated on the rGO sheets.

Figure 3 illustrates the synthesis of GO, rGO and rGO-Ag composites. As explained in the experimental section, steps 1, 2, and 3 in Fig. 3 are the preparation of GO by Hummers method, synthesis of Ag seeds decorated rGO sheets, and rGO by MW irradiation, respectively. Steps 4, 5 & 6 are for the formation of rGO-Ag composites. With the addition of different ILs, the growth of different silver nanostructures decorated over rGO sheets are guided. This is explained through the two possible mechanisms (1) anions exchange reactions between the anion in ILs and NO_3^- ions of silver nitrate precursor, and (2) the surfactant nature of ILs used in the synthesis. The strength of anion exchange reactions is reliant on the type of ions (cations and anions) that combine to make IL and the interaction energy of involved ions. The interaction energy is mostly contributed by the long-range electrostatic attractions. The ILs having more interaction energy are difficult to make exchange reactions, and it relies on the parameters such as size, shape and distribution of charges on ions. In the case of imidazolium based ILs, the interaction energy is also decided by alkyl chain length of the cation [42]. In the preparation of rGO-Ag1composite, ILs are not used to modify morphology of silver, which resulted to form nanoparticles/rods (step 4 in the Fig. 3). Nanoparticles are evenly distributed over rGO in rGO-Ag2 and rGO-Ag3and the absence of nanowires/rods are observed (step 5 in Fig. 3). Anions involved in the synthesis of rGO-Ag2 and rGO-Ag3 are BF_4 and TFA which
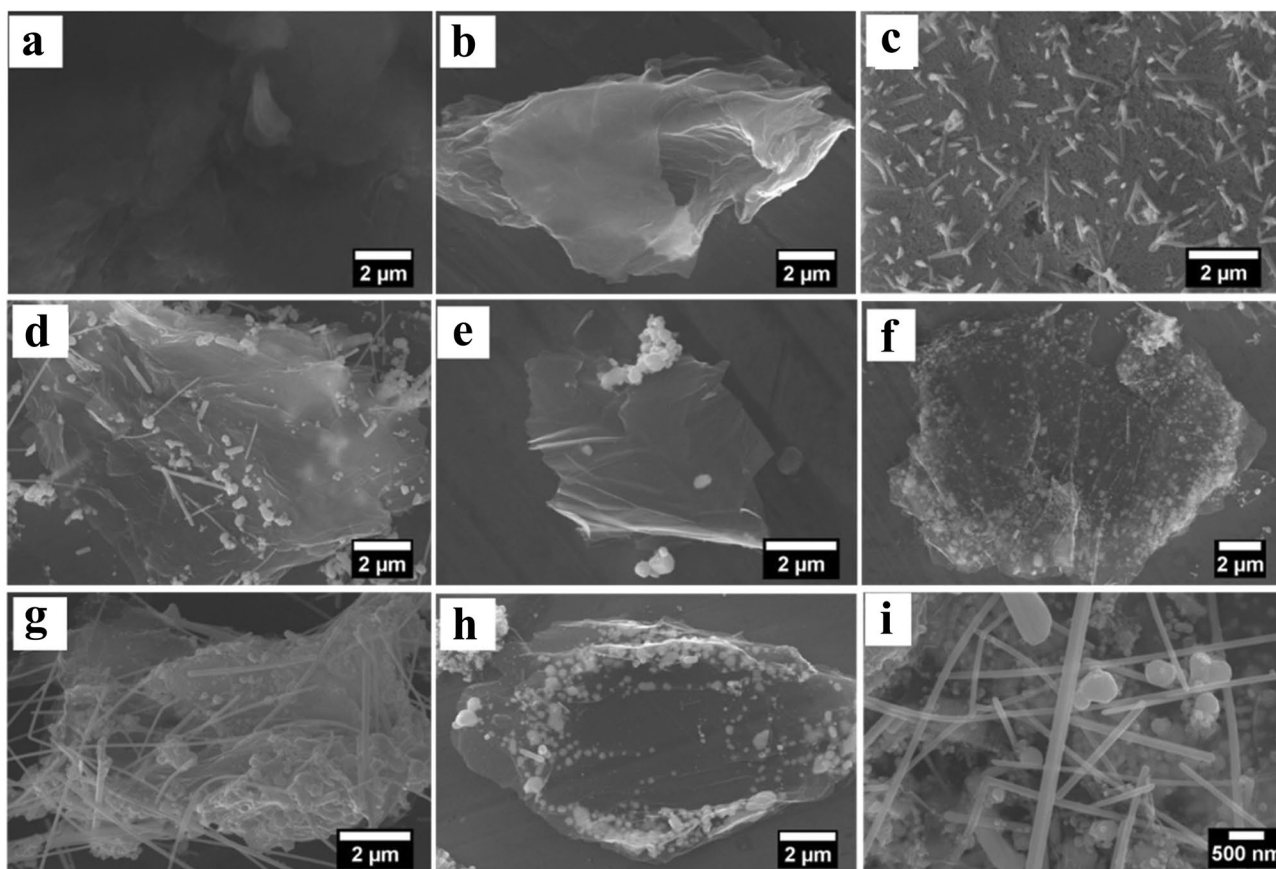

Fig. 2 FE-SEM images of **a** GO, **b** rGO, **c** Ag, **d** rGO-Ag1, **e** rGO-Ag2, **f** rGO-Ag3, **g** rGO-Ag4, **h** rGO-Ag5 and **i** rGO-Ag4 (at higher magnification)
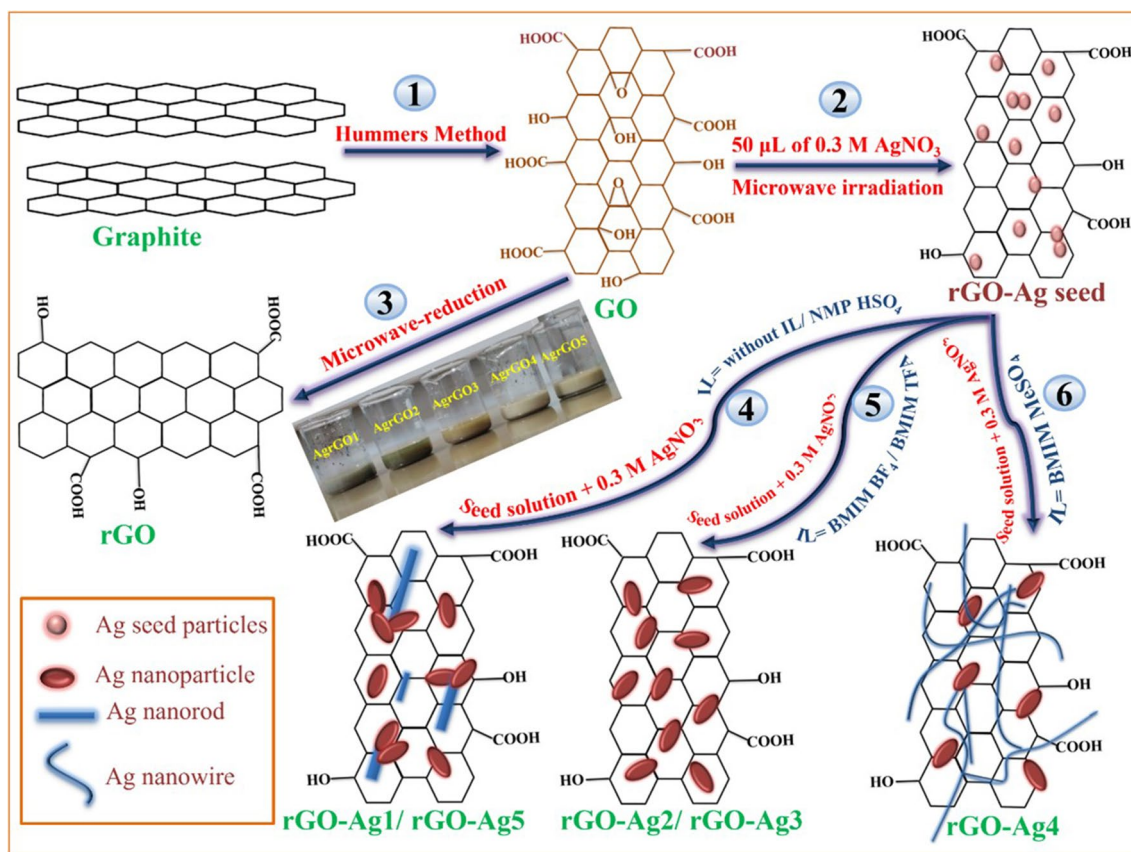
Fig. 3 Schematic illustrations for the synthesis of GO, rGO and their silver composites

have lesser interaction energies with BMIM cation compared to NO_3^- ion. This resulted in the formation of BMIM NO_3 by anion exchange interaction. Native anions of BF_4 and TFA are replaced by the NO_3^- ions. Dissociated anions of BF_4 and TFA are decomposed to give F^- ions which interact with Ag^+ ions to form AgF. Highly reacting F^- ions are deposited on the {111} facets of the multipletwined seed crystals which arrests the growth in {111} direction. In addition, AgF formed in multiple nucleating sites on rGO restricts the growth of rods/wire as well as reduces the size of silver nanoparticles. The formation of AgF is established from the emergence of a peak at $2\theta = 31.46°$ in the powder XRD pattern of rGO-Ag2 and rGO-Ag3, which corresponds to (111) plane of FCC AgF (JCPDS card no. 72–1535). The rGO-Ag4 composite has lengthy nanowires grown from the nanoparticles decorated on rGO (step 6 in the Fig. 3). Here, the anion exchange interactions are not possible, because the interaction energy is high between the $MeSO_4$ anion and BMIM cation, NO_3 ions are not able to replace the native $MeSO_4$ anion. As mentioned, BMIM $MeSO_4$ acts as an additional surfactant along with PVP to enhance 1D growth of silver nanowires. The surface energy of FCC metal crystal facets are in the order as {110} > {100} > {111} and stability follows the reverse order [43]. PVP attached to{100}

facets arrests the growth in that direction, leading to the formation of 1D growth. ILs are more interacting with high surface energy facets of the metal crystals, and it covers {110} facets of wires, which avoids the deposition of more Ag^+ ions on {110} facet. Thus, {111} facets are not affected by ILs as well as PVP that allows the Ag atoms to deposit on {111} facet, enhancing the growth to form long nanowires. In the sample, rGO-Ag5 silver nanoparticles and nanorods are decorated over the rGO sheets, which supports the poor anion exchange reaction (step 4 in Fig. 3). The strong interaction between HSO_4 anion with pyrrolidone cation prevents the exchange interaction. Despite this, it fails to support the growth of wires due to the poor surfactant nature of NMP HSO_4. Based on these results, morphology of silver metal can be tuned with the help of different ILs in a microwave irradiation method.

The inhibitor efficiency of the samples GO, rGO, Ag and rGO-Ag composites against A549 cancer cells and their cell viability analysis results are given in Fig. 4. The IC_{50} concentrations values are estimated as 180 µg/mL, 140 µg/mL, 20 µg/mL, 50 µg/mL, 22 µg/mL, 20 µg/mL, 32 µg/mL and 34 µg/mL for the samples GO, rGO, Ag and rGO-Ag1, rGO-Ag2, rGO-Ag3, rGO-Ag4 and rGO-Ag5, respectively. At lower concentrations, GO/rGO samples show reduced
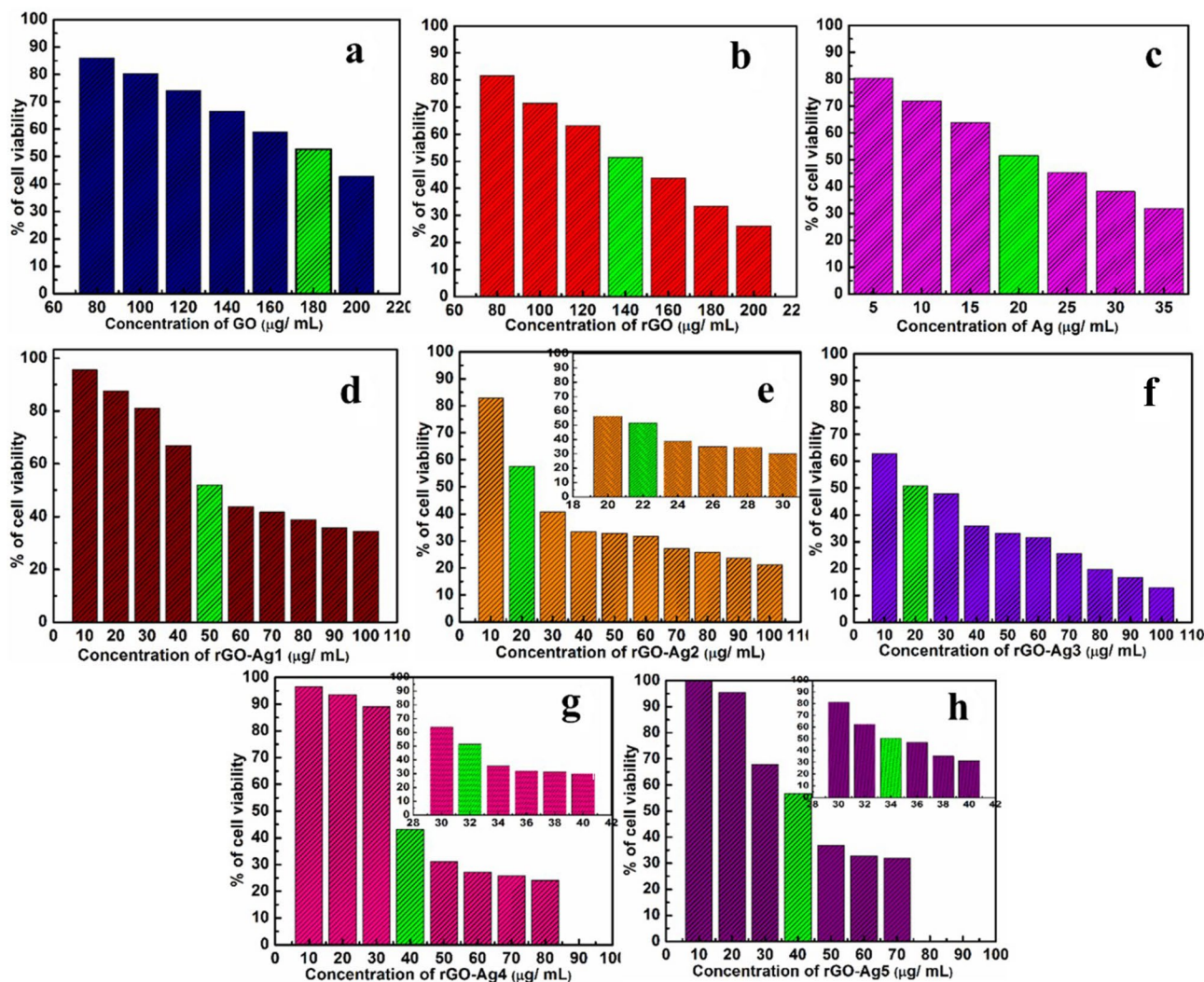
Fig. 4 In-vitro cytotoxicity results of the prepared samples against A549 cells. The bars with green shading are corresponding to the IC_{50} concentration of the prepared samples **a** GO, **b** rGO, **c** Ag, **d** rGO-Ag1, **e** rGO-Ag2, **f** rGO-Ag3, **g** rGO-Ag4 and **h** rGO-Ag5

cytotoxicity against the cancer cells. With improved concentrations, GO/rGO shows higher toxicity against cancer cells due to the oxidative stress produced in cancer cells. The sample Ag shows improved toxicity by the effective diffusion of small size Ag particles into the intracellular region through cell membrane in the endocytosis process. Bare Ag shows highest toxicity due to the effective release of Ag^+ ions to intracellular region. Nanoparticles in the intracellular region are triggers to produce excess ROS, which are the major cause to begin apoptosis. Among the tested samples, Ag and rGO-Ag3 have the highest cytotoxicity ($IC_{50}=20$ µg/mL) against A549 lung cancer cells. In the case of rGO-Ag3, the size of Ag particles decorated over rGO are small, and no agglomeration was observed which minimizes the loading of Ag particles on rGO. The average size of Ag nanoparticles on rGO are calculated to be 270 nm, 82 nm, 75 nm, 220 nm, and 290 nm for rGO-Ag1-5, respectively. It is also evidenced

that the cytotoxicity relatively increased with the decreased particle size.

Various mechanisms are involved in the apoptosis-based cell death induced by AgNPs like the destruction of cell membrane, ROS production, and DNA damage. Ag^+ ions released from AgNPs involved the oxidization of glutathione and rises the peroxidation of lipids in cellular membranes. It leads to the destruction of cellular membrane and subsequent leaking of cytoplasmic constituents from the injured cells. Heavy metals catalyzed Haber–Weiss reactions are taking place inside cells leading to the formation of highly reactive ROS like ·OH radicals from H_2O_2. These free radicals are affecting the mitochondrial respiratory chain by defeating ATP production pathway leading to cell death. This stops the electron transport chain and will lead to the beginning of apoptosis. Hydroxide radicals are directed to mitochondrial outer membrane permeabilization and release hemeprotein

cytochrome c to the cytosol. Apart from these two methods, DNA damage is the potential cause of apoptosis. The basic structure of DNA is built from the four nucleic acids, adenine (A), guanine (G), cysteine (C), and thymine (T). These bases are making complementary pairs as G≡C and A = T through hydrogen bonding [44]. Ag$^+$ ions destruct the hydrogen bonding by making bonding with the above mentioned nucleic acids. Ag atoms are make twofold coordinate linear bonds with N to form O = Ag$^+$-N, N-Ag$^+$-N, and N = Ag$^+$-O in G≡C pair, and N-Ag$^+$-O and N-Ag$^+$-N in A = T pair. These Ag-based coordination bonds highly damage the DNA, leading to apoptosis.

AO/EB dual stain was used to study the cell damage by apoptosis and chromatin condensation of A549 lung cancer cells treated with rGO-Ag samples with their respective IC$_{50}$ concentrations and the results are shown in Fig. 5. AO/EB combined stain will give light green fluorescence for alive cells, bright fluorescence for initial apoptotic cells, orange fluorescence for late apoptotic cells and dark red spots for the dead cells. From the results shown in Fig. 5, the sample rGO-Ag3 treated cells has fewer green spots compared to others and shows small condensed red spots corresponding to more membrane damage and cell death. The results are reliable with the cytotoxicity results of the samples against A549 cells.

From the above results, it is established that the synthesized rGO-Ag samples are showing cytotoxicity against A549 lung cancer cells. The cytotoxicity is through apoptosis process initiated by ROS initiated with Ag$^+$ ions released from silver nanoparticles/wires decorated on rGO. Higher accumulation of ROS results in oxidative stress and interruptions in cell functions leads to apoptosis. The dye 2′, 7′ dichlorofluorescein-diacetate (DCFH-DA) was used to spot the intracellular ROS production. Unoxidized DCFH-DA is a non-fluorescent one, while it is oxidized by •OH radicals highly fluorescent DCF was formed. The increased fluorescence in nanomaterials treated cells are indications of higher ROS in cells. Figure 6 shows the DCFH-DA treated A549 cells. The images in Fig. 6a–i are for the cells treated with control cells, GO, rGO, Ag, rGO-Ag1, rGO-Ag2, rGO-Ag3, rGO-Ag4 and rGO-Ag5, respectively with their IC$_{50}$ concentrations. Compared to the control (Fig. 6a) all others exhibit a higher intensity fluorescence, which indicates the increased production of ROS in the apoptotic cells.

Hoechst 33,258 fluorochrome dye can diffuse through both viable/nonviable cells and binds with DNA minor groove at
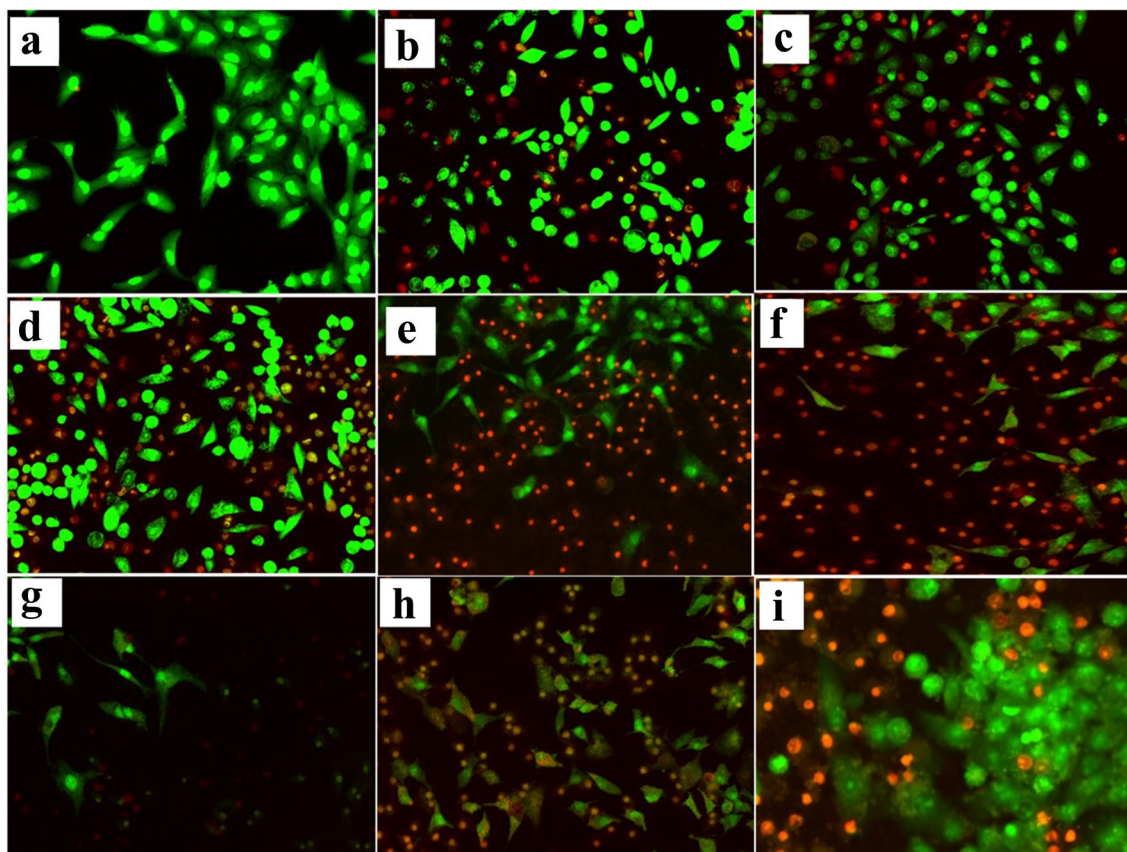

Fig. 5 Morphological changes of A549 lung cancer cells after treatment with **a** control, **b** GO, **c** rGO, **d** Ag, **e** rGO-Ag1, **f** rGO-Ag2, **g** rGO-Ag3, **h** rGO-Ag4 and **i** rGO-Ag5 composites studied with the help of AO/EB dual staining
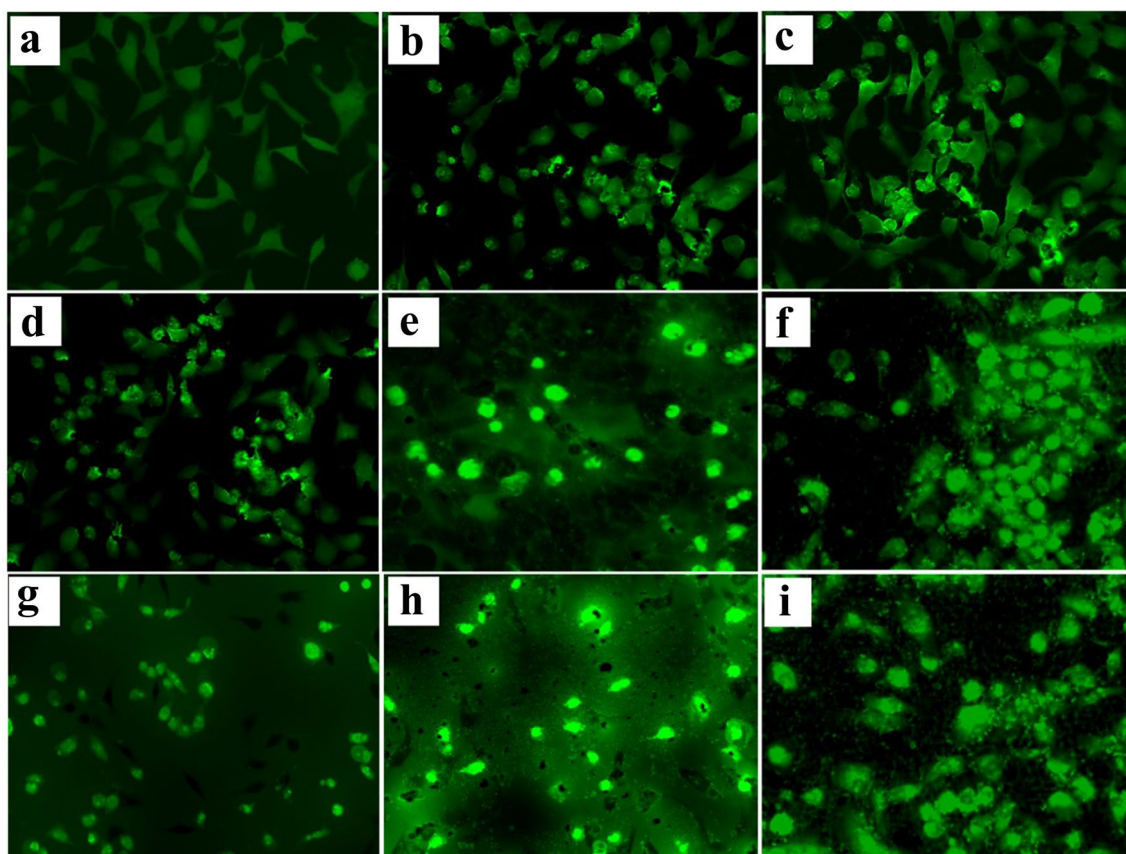
Fig. 6 Level of ROS in the A549 cells **a** control, **b** GO, **c** rGO, **d** Ag, **e** rGO-Ag1, **f** rGO-Ag2, **g** rGO-Ag3, **h** rGO-Ag4 and **i** rGO-Ag5

A-T rich regions giving a broad spectrum of blue fluorescence at 460 nm. Fluorescent images of Hoechst 33,258 treated lung cancer A549 cells are shown in the above Fig. 7. The Hoechst 33,258 gives weak fluorescence in normal cells (Fig. 7a), an intense spherical fluorescence for the chromatin condensed cells, and nuclear-fragmented products were observed. The fluorescence images of GO, rGO, Ag, rGO-Ag1, rGO-Ag2, rGO-Ag3, rGO-Ag4 and rGO-Ag5 composites treated A549 cells with their respective IC_{50} concentrations are shown in Fig. 7b–i, respectively. Except for the control cells, all the nanocomposites treated cells showed intense fluorescence, and shrunken nuclear size was noted, as a result of apoptosis. Caspase-3 induced chromatin condensation is the signature of earlier apoptosis-based cell death. More nucleus condensation and fragmentation were observed in Ag and rGO-Ag composites treated cells, this evidenced that the cell death is a result of apoptosis.

4 Conclusion

In this work, composites with tunable size and morphologies of silver nanostructures decorated on rGO sheets in a rapid microwave synthesis method are reported in detail. ILs are used to tune the size and morphology of silver nanostructures and it depends on anion exchange interaction between IL native anion and NO_3 ions in $AgNO_3$ precursor. Cytotoxicity of the samples against A549 cells indicates that the composite rGO-Ag3 shows highest toxicity against lung cancer cells with IC_{50} value of 20 µg/mL. Based on the results, the prepared composites can be used as potential chemo drugs against A549 cells. The results obtained from this study open a new avenue to prepare rGO-metal based nanocomposites with tunable morphologies using ILs. The Ag nanoparticle loading and decorations on rGO are controlled by ILs treatment, which enhanced the anticancer activity of rGO-Ag composites. It also motivates us to study the cytotoxicity properties of prepared composites against different cancer cells in near future.
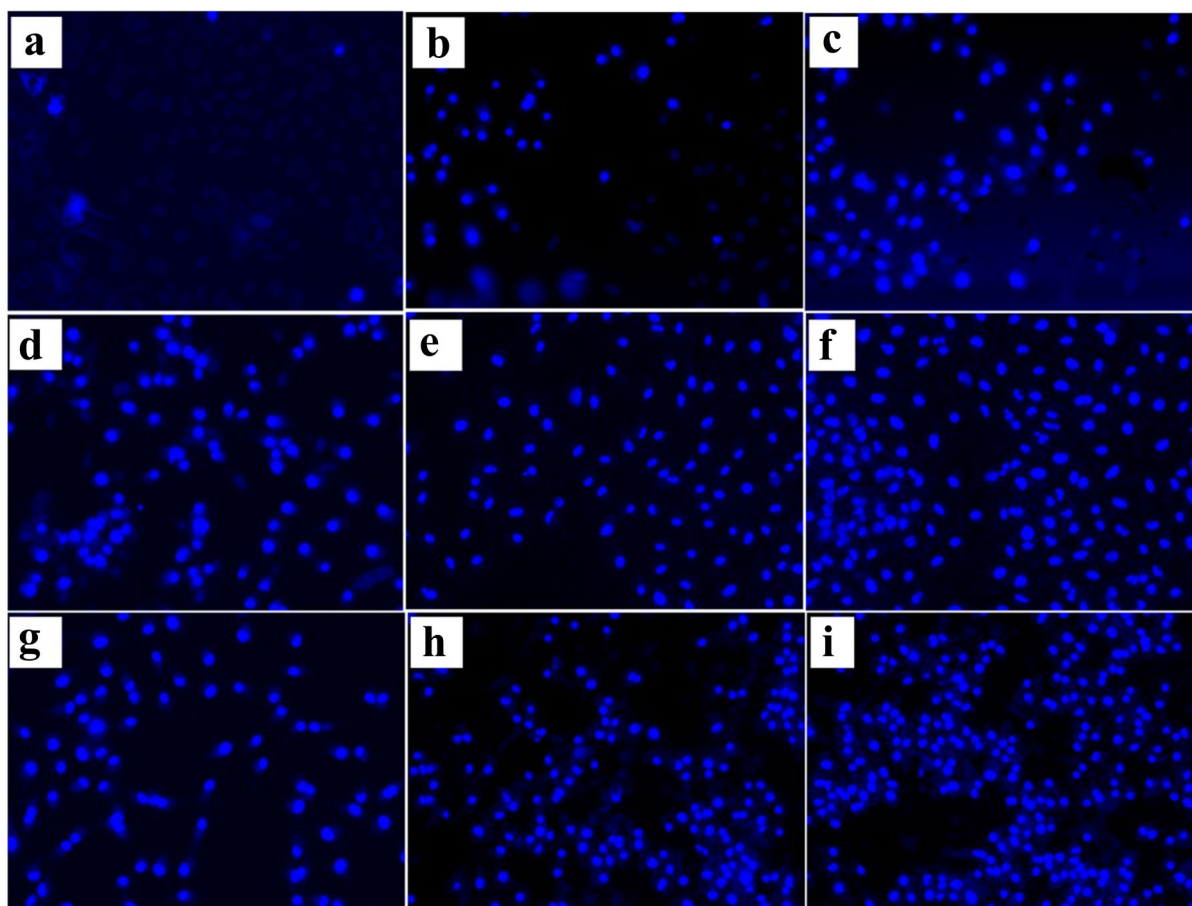
Fig. 7 Nuclear staining analyses of A549 cells treated with the IC_{50} concentrations of the prepared samples treated cells **a** control cells, **b** GO, **c** rGO, **d** Ag, **e** rGO-Ag1, **f** rGO-Ag2, **g** rGO-Ag3, **h** rGO-Ag4 and **i** rGO-Ag5

Author Contributions The corresponding author SM: Conceptualization, data curation, resources, investigations, writing- original draft, writing- reviews and editing and supervision. The first author KL: conceptualization, data curation, investigation writing-original draft, writing- revision and editing. SP: anti-cancer activity studies and writing. VR: anticancer activity studies and writing.

Data Availability The datasets generated during and/or analyzed during the current study are available from the corresponding author on reasonable request.

Declarations

References

1. J. Ferlay, M. Colombet, I. Soerjomataram, D.M. Parkin, M. Piñeros, A. Znaor, F. Bray, Int. J. Cancer **149**, 778 (2021)
2. C. Zappa, S.A. Mousa, Transl. Lung Cancer Res. **5**, 288 (2016)
3. S. Ramalingam, C. Belani, Oncologist **13**, 5 (2008)

4. M. Oves, M. Aslam, M.A. Rauf, S. Qayyum, H.A. Qari, M.S. Khan, M.Z. Alam, S. Tabrez, A. Pugazhendhi, I.M.I. Ismail, Mater. Sci. Eng. C **89**, 429 (2018)

5. Y. Liu, Q. Shi, C. Hou, Q. Zhang, Y. Li, H. Wang, Carbon N. Y. **125**, 352 (2017)

6. G. Anagnostopoulos, P.N. Pappas, Z. Li, I.A. Kinloch, R.J. Young, K.S. Novoselov, C.Y. Lu, N. Pugno, J. Parthenios, C. Galiotis, K. Papagelis, A.C.S. Appl, Mater Interf **8**, 22605 (2016)

7. A.V. Naumov, Graphene Oxide Fundam. Appl. **2016**, 147 (2016)

8. Q. Ke, J. Wang, J. Mater. **2**, 37 (2016)

9. M. Ye, Z. Zhang, Y. Zhao, L. Qu, Joule **2**, 245 (2018)

10. L.R. Shobin, S. Manivannan, Sens Actuators B Chem. **220**, 1178 (2015)

11. N. Panwar, A.M. Soehartono, K.K. Chan, S. Zeng, G. Xu, J. Qu, P. Coquet, K.T. Yong, X. Chen, Chem. Rev. **119**, 9559 (2019)

12. C. Cheng, S. Li, A. Thomas, N.A. Kotov, R. Haag, Chem. Rev. **117**, 1826 (2017)

13. L. Xu, Y.Y. Wang, J. Huang, C.Y. Chen, Z.X. Wang, H. Xie, Theranostics **10**, 8996 (2020)

14. D. Ficai, A. Ficai, E. Andronescu, Nanomater. Toxic. Risk Assess. (2015). https://doi.org/10.5772/60665

15. G.A. Sotiriou, S.E. Pratsinis, Curr. Opin. Chem. Eng. **1**, 3 (2011)

16. Y.M. Que, X.Q. Fan, X.J. Lin, X.L. Jiang, P.P. Hu, X.Y. Tong, Q.Y. Tan, RSC Adv. **9**, 21134 (2019)

17. P.L. Drake, K.J. Hazelwood, Ann. Occup. Hyg. **49**, 575 (2005)

18. V. Georgakilas, M. Otyepka, A.B. Bourlinos, V. Chandra, N. Kim, K.C. Kemp, P. Hobza, R. Zboril, K.S. Kim, Chem. Rev. **112**, 6156 (2012)

19. T. Kavinkumar, K. Varunkumar, V. Ravikumar, S. Manivannan, J. Coll. Interf. Sci. **505**, 1125 (2017)

20. G. Darabdhara, M.R. Das, S.P. Singh, A.K. Rengan, S. Szunerits, R. Boukherroub, Adv. Coll. Interf. Sci. **271**, 101991 (2019)

21. A.V.A. Mariadoss, K. Saravanakumar, A. Sathiyaseelan, M.H. Wang, J. Photochem. Photobiol. B Biol. **210**, 111984 (2020)

22. P. Gnanaprakasam, T. Selvaraju, RSC Adv. **4**, 24518 (2014)

23. S.M. Li, Y.S. Wang, S.T. Hsiao, W.H. Liao, C.W. Lin, S.Y. Yang, H.W. Tien, C.C.M. Ma, C.C. Hu, J. Mater. Chem. C **3**, 9444 (2015)

24. Q.T. Tran, M.H.H. Tran, D.T. Tong, V.T. Tran, N.D. Nguyen, Adv. Nat. Sci. Nanosci. Nanotechnol. **4**, 2 (2013)

25. K. Lakshmanamoorthy, S. Manivannan, J. Mater. Sci. Mater. Electron. **33**, 8724 (2022)

26. M.T. Rahman, M.F. Kabir, A. Gurung, K.M. Reza, R. Pathak, N. Ghimire, A. Baride, Z. Wang, M. Kumar, Q. Qiao, A.C.S. Appl, Nano Mater. **2**, 4842 (2019)

27. Z. Lei, B. Chen, Y.M. Koo, D.R. Macfarlane, Chem. Rev. **117**, 6633 (2017)

28. C. Janiak, Top. Organomet. Chem. **51**, 17 (2015)

29. A. Chinnappan, R. Appiah-Ntiamoah, W.J. Chung, H. Kim, Int. J. Hydrogen Energy **41**, 14491 (2016)

30. W.S. Hummers Jr., R.E. Offeman, J. Am. Chem. Soc. **80**, 1339 (2002)

31. J.D. Holbrey, W.M. Reichert, R.P. Swatloski, G.A. Broker, W.R. Pitner, R. Seddon, R.D. Rogers, Green chem. **4**, 407 (2002)

32. W. Wang, L. Shao, W. Cheng, J. Yang, M. He **9**, 337 (2008)

33. S. Nehrer, H.A. Breinan, A. Ramappa, H.P. Hsu, T. Minas, S. Shortkroff, C.B. Sledge, I.V. Yannas, M. Spector, Biomaterials **19**, 2313 (1998)

34. Z.B. Wang, Y.Q. Liu, Y.F. Cui, Cell Biol. Int. **29**, 489 (2005)

35. E. Ulukaya, C. Acilan, Y. Yilmaz, Cell Biochem. Funct. **29**, 468 (2011)

36. M.B. Gebeyehu, T.F. Chala, S.Y. Chang, C.M. Wu, J.Y. Lee, RSC Adv. **7**, 16139 (2017)

37. R. Bryaskova, D. Pencheva, S. Nikolov, T. Kantardjiev, J. Chem. Biol. **4**, 185 (2011)

38. V. Ţucureanu, A. Matei, A.M. Avram, Crit. Rev. Anal. Chem. **46**, 502 (2016)

39. J. Guerrero-Contreras, F. Caballero-Briones, Mater. Chem. Phys. **153**, 209 (2015)

40. N. Kumar, V.C. Srivastava, ACS Omega **3**, 10233 (2018)

41. F. Tuinstra, J.L. Koenig, J. Chem. Phys. **53**, 1126 (1970)

42. P. Naert, K. Rabaey, C.V. Stevens, Green Chem. **20**, 4277 (2018)

43. H.Y. Wang, Y.A. Gao, M.W. Zhao, L.Q. Zheng, Chinese Chem. Lett. **21**, 872 (2010)

44. T. Ishida, MOJ Tumor Res. **1**, 8 (2017)